Crystal Structures of Acetylcholinesterase in Complex with Organophosphorus Compounds Suggest that the Acyl Pocket Modulates the Aging Reaction by Precluding the Formation of the Trigonal Bipyramidal Transition State[†,‡]

Andreas Hörnberg, Anna-Karin Tunemalm, and Fredrik Ekström*

FOI CBRN Defence and Security, S-901 82 Umeå, Sweden

Received October 13, 2006; Revised Manuscript Received February 6, 2007

ABSTRACT: Organophosphorus compounds (OPs), such as nerve agents and a group of insecticides, irreversibly inhibit the enzyme acetylcholinesterase (AChE) by a rapid phosphorylation of the catalytic Ser203 residue. The formed AChE−OP conjugate subsequently undergoes an elimination reaction, termed aging, that results in an enzyme completely resistant to oxime-mediated reactivation by medical antidotes. In this study, we present crystal structures of the non-aged and aged complexes between *Mus musculus* AChE (mAChE) and the nerve agents sarin, VX, and diisopropyl fluorophosphate (DFP) and the OP-based insecticides methamidophos (MeP) and fenamiphos (FeP). Non-aged conjugates of MeP, sarin, and FeP and aged conjugates of MeP, sarin, and VX are very similar to the noninhibited apo conformation of AChE. A minor structural change in the side chain of His447 is observed in the non-aged conjugate of VX. In contrast, an extensive rearrangement of the acyl loop region (residues 287−299) is observed in the non-aged structure of DFP and in the aged structures of DFP and FeP. In the case of FeP, the relatively large substituents of the phosphorus atom are reorganized during aging, providing a structural support of an aging reaction that proceeds through a nucleophilic attack on the phosphorus atom. The FeP aging rate constant is 14 times lower than the corresponding constant for the structurally related OP insecticide MeP, suggesting that tight steric constraints of the acyl pocket loop preclude the formation of a trigonal bipyramidal intermediate.

The enzyme acetylcholinesterase (AChE)[1] terminates cholinergic transmission by rapidly hydrolyzing the signal substance acetylcholine. Certain organophosphorus compounds (OPs) such as the nerve agents and a group of insecticides interfere with the catalytic mechanism of AChE by forming covalently attached phosphorus conjugates with the catalytic residue Ser203. These phosphorus conjugates lead to inhibition of the natural activity of the enzyme (Figure 1A). Treatment of the AChE−OP conjugate with oxime-based medical antidotes, substances also known as reactivators, can in many cases restore the function of the inhibited enzyme. The efficiency of the reactivation reaction depends on several factors such as the chemical structure of the OPs and the reactivator as well as the sequence of the inhibited AChE. For instance, conjugates between human AChE (hAChE) and OP compounds such as tabun, DFP, and FeP exhibit a high resistance toward reactivation, whereas conjugates of VX, sarin, and MeP can be readily reactivated by a number of different reactivators (*2*). It has also been shown that both the inhibition and reactivation kinetics are highly dependent on the stereochemistry of the organophosphorus conjugate (*3*−*8*). The analysis of kinetic constants is further complicated by significant species dependence (*9*, *10*). The reactivation reaction can also proceed without the presence of an oxime-based reactivator, a phenomenon known as spontaneous reactivation (Figure 1A). The majority of AChE−OP conjugates undergo spontaneous reactivation at a negligible rate. However, the MeP conjugate is a striking exception with a half-time of ∼3 h in hAChE (*2*).

Another time-dependent fate of the AChE−OP conjugate is an elimination reaction termed "aging" that usually involves dealkylation or deamidation of the phosphorus conjugate (Figure 1A). The aging reaction results in a very stable anionic AChE−OP conjugate that is completely resistant toward reactivation with the oxime-based reactivators known today. The variability in the rate of aging is pronounced; for example, the aging half-time of hAChE

[†] This work was supported by the Swedish Armed Forces Research and Technology Program. A.H. is supported by a grant from the Swedish Emergency Management Agency.

[‡] PDB entries 2JGE, 2JGF, 2JGG, 2JGH, 2JGI, 2JGJ, 2JGK, 2JGL, and 2JGM are for the mAChE conjugates with MeP, FeP, sarin, VX, DFP, AMeP, AFeP, AVX/sarin, and ADFP, respectively.

* To whom correspondence should be addressed. E-mail: fredrik.ekstrom@foi.se. Telephone: +46-90-106815. Fax: +46-90-106809.

[1] Abbreviations: AChE, acetylcholinesterase; apo, nonconjugated AChE [PDB entry 1J06 (*1*)]; DTNB, 5,5′-dithiobis(2-nitrobenzoic acid); DFP, diisopropyl fluorophosphate; HI-6, 1-(2-hydroxyiminomethylpyridinium)-1-(4-carboxyamino)pyridinium dimethyl ether dichloride; mAChE, *Mus musculus* acetylcholinesterase; MEPQ, 7-(*O*-ethylmethylphosphinyloxy)-1-methylquinolinium iodide; OP, organophosphorus compound; rmsd, root-mean-square deviation; sarin, methylethyl methylphosphonofluoridate; Ortho-7, 1,7-heptylene-bis-*N*,*N*′-2-pyridiniumaldoxime dichloride; soman, 1,2,2-trimethylpropyl methylphosphonofluoridate; tabun, ethyl *N*,*N*-dimethylphosphoramidocyanidate; TcAChE, *Torpedo californica* acetylcholinesterase; VX, *O*-ethyl *S*-2-isopropylaminoethyl methylphosphonothiolate. The sequence numbering of mAChE is used throughout this paper when amino acids of any AChE are discussed.

10.1021/bi0621361 CCC: $37.00
Published on Web 04/03/2007

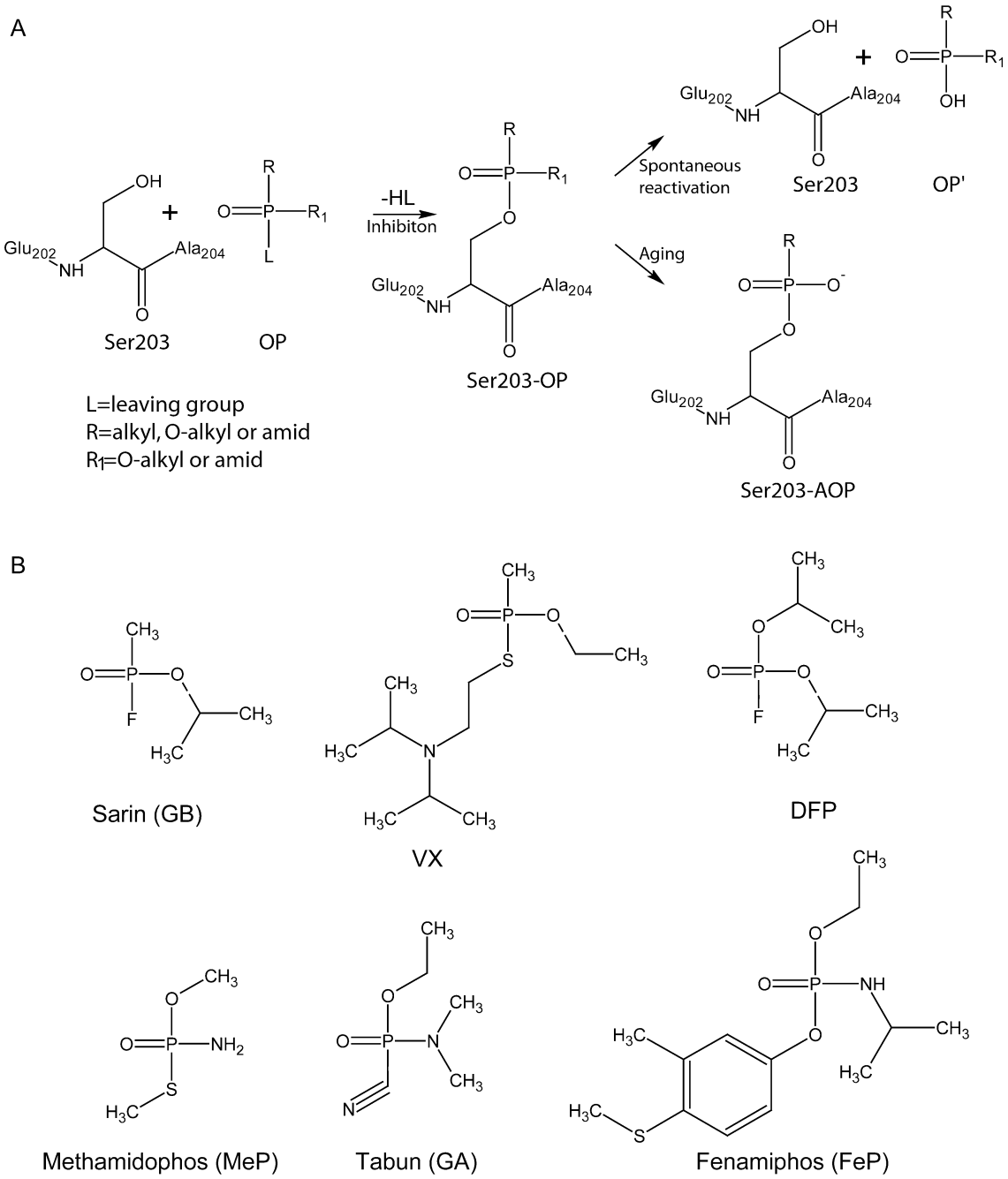

FIGURE 1: Scheme describing the inhibition, aging, and spontaneous reactivation of AChE inhibited by organophosphorus compounds (A). Chemical structure of some nerve agents and insecticides discussed in this study (B). Bonds connecting the first leaving group are marked with a gray wavy line, whereas bonds cleaved during the aging reaction are marked with a gray dotted line. In the case of sarin, VX, and DFP, the exact position of bond cleavage is not known. The aging product of methamidophos and fenamiphos is not known.

inhibited by soman is a few minutes as compared to the quite stable conjugates of fenamiphos with a half-time of more than 130 h (*2*).

The catalytic site of AChE is located close to the base of a narrow active site gorge that extends ~20 Å into the enzyme (*11*). The catalytic triad (Glu334-His447-Ser203) is found at the bottom of the active site gorge, surrounded by three structural features important for catalytic activity: the acyl pocket (residues Phe295, Phe297, and Phe338), the oxyanion hole (main chain nitrogen from residues Gly121, Gly122, and Ala204), and the choline-binding site (Trp86 and Tyr337). Crystallographic studies of the non-aged form of *Torpedo californica* acetylcholinesterase (*Tc*AChE) inhibited by VX (*Tc*AChE−VX) have shown that the side chain of His447 undergoes a structural change that disrupts the catalytic triad (*12*). A similar structural change of His447 has been described in a recent crystal structure of non-aged mAChE inhibited by tabun (mAChE−tabun) (*13*). Furthermore, the tabun conjugate induces a distortion of the side chain of Phe338 to a position in the narrow active site gorge. Additional crystallographic analysis of the interaction between the reactivator HI-6 and nonphosphorylated mAChE has shown that the structural change of Phe338 in mAChE−tabun is likely to perturb the binding site of HI-6 (*14*). This finding implies that the distortion of Phe338 observed in the non-aged structure of mAChE−tabun contributes to the high resistance of tabun conjugates toward reactivation. The structural distortions that the VX and tabun conjugates induce

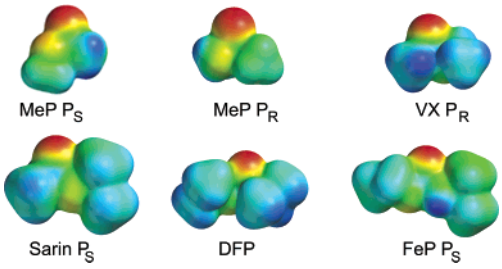

FIGURE 2: Molecular models showing the overall size and shape of the non-aged form of the OP compounds. The colors indicate the electrostatic potential where red corresponds to negative potential and blue to positive potential. The models are positioned with a fictitious "serine oxygen−phosphorus bond" pointing inward. To simplify the calculations and visualization of these models, the protein is replaced with a methoxy group. The models are purely used as a comparison within this group of models, and the quantitative values are not considered.

are reversed upon aging, and the aged structures are very similar to their apo structures (*Tc*AChE-apo and mAChE-apo, respectively).

In this study, we describe the non-aged and aged crystal structures of mAChE in complex with the nerve agents sarin (mAChE−sarin and mAChE−AVX/sarin), VX (mAChE−VX and mAChE−AVX/sarin), and DFP (mAChE−DFP and mAChE−ADFP). We also investigate the mAChE conjugates of the OP-based insecticides methamidophos (mAChE−MeP and mAChE−AMeP) and fenamiphos (mAChE−FeP and mAChE−AFeP). The OPs described in this study exhibit diversity in the sizes and electronic properties in their substituents (Figures 1B and 2). They also represent a high degree of diversity in their resistance toward reactivation, their rate of spontaneous reactivation, and their rate of aging (*2*).

MATERIALS AND METHODS

As some of the compounds in this study are highly toxic and belong to Schedule 1 Chemicals as defined in the Chemical Weapons Convention, all work with such substances is regulated by the Convention. The handling of sarin, VX, and DFP is dangerous and requires suitable personal protection, training, and facilities.

Cloning, Expression, Crystal Screening, and Generation of AChE−OP Complexes. Cloning, expression, purification, and crystal screening of mAChE were performed as previously described (*13*). The non-aged complexes were generated by crystal soaking methods. Crystals were slowly allowed to equilibrate in X-buffer composed of 28% (v/v) polyethylene glycol monomethyl ether 750 and 100 mM HEPES (pH 7.0). Prior to data collection, X-buffer was supplemented with the appropriate OP compound at a concentration of 10 mM for sarin, VX, and DFP and 100 mM for methamidophos and fenamifos. The solution was subsequently added to the equilibrated crystals in several (5−10) portions of 0.5 μL during a period of 30−120 min (30 min for sarin and DFP). In the case of MeP, sarin (which has an aging product identical to that of VX), and FeP, aged complexes were generated by inhibition of mAChE with OPs prior to crystallization, whereas aged complexes of DFP were produced by incubating DFP-soaked crystals. Fenamiphos and methamidophos were allowed to age for 10 weeks; sarin was aged for 3 weeks, and DFP-inhibited crystals were aged for 30 h prior to data collection. In all cases, complete inhibition was verified by measurements of the residual AChE activity on dissolved crystals.

Collection, Processing, and Refinement of Diffraction Data. Crystals were flash-frozen in liquid nitrogen, and X-ray diffraction data were collected at 100 K at the MAXlab synchrotron (Lund, Sweden), beamline I711, on a MAR Research CCD detector. Images were collected with an oscillation angle of 1.0° per exposure, and the total oscillation range covered at least 160° per data set. Intensity data were indexed and integrated with XDS (*15*) and scaled using Scala (*16*). The structure was determined using rigid body refinement with the apo structure of mAChE as a starting model (PDB entry 1J06) (*1*). Further crystallographic refinement was carried out using restrained isotropic *B*-factor refinement as implemented in Refmac5 (*17*). Refinement included 98% of the data, whereas the remaining 2% was excluded and used to follow the progress of the refinement with R_{free} (*18*). The R_{free} data set (2%) was obtained from a previously determined structure (PDB entry 2GYU) and was used for all structures in this study to prevent model bias. Several rounds of refinement were performed, alternating with manual rebuilding of the model after visualization of $2|F_o| - |F_c|$ and $|F_o| - |F_c|$ maps using O (*19*). The quality of the final model was evaluated using PROCHECK and WHATCHECK (*20*, *21*), and root-mean-square deviations (rmsd) were calculated using LSQMAN. Figures were made using PyMol and MOLRAY (*22*).

For calculations of the molecular surfaces (Figure 2), ab initio calculations were performed using Spartan (Wavefunctions Inc.). The purpose of the molecular surface models is to give a visual picture of diversity in size, shape, and electrostatic potential of the OP compounds. They are to be used for comparison within this group only. Hence, the Hartree−Fock 3-21G* basis set was considered sufficient for the generation of the models. In the inhibited enzyme, the phosphorus atom of the conjugate forms a covalent bond to Oγ of Ser203. For these calculations, Ser203 was approximated with a methoxy group by exchanging the P−Oγ bond to Ser203 with a P−OMe bond, giving primitive models that do not undertake the interaction between amino acids in the vicinity of the OP compounds.

RESULTS

General Features and Quality of the Final Models. The overall structures of OP-inhibited mAChE are very similar to the apo structure of mAChE (*1*) with minor structural distortions of the catalytic site (discussed in detail in the following sections). The asymmetric unit contains two monomers (A and B), of which the A monomer is better resolved in the electron density map, and also display lower atomic *B*-factors. The loop region between residues 258 and 265 could not be traced in the electron density map, as previously described for the apo structure (*1*). In all structures, we observe a strong, positive electron density feature in the initial $|F_o| - |F_c|$ map 1.6 Å from Oγ of Ser203, which is accredited to the covalently bound phosphorus atom of the OP compound. The overall coordination of the conjugates is very similar, with the phosphonyl O1 within hydrogen bonding distance of the main chain amide nitrogen of Gly121, Gly122, and Ala204, i.e., the oxyanion

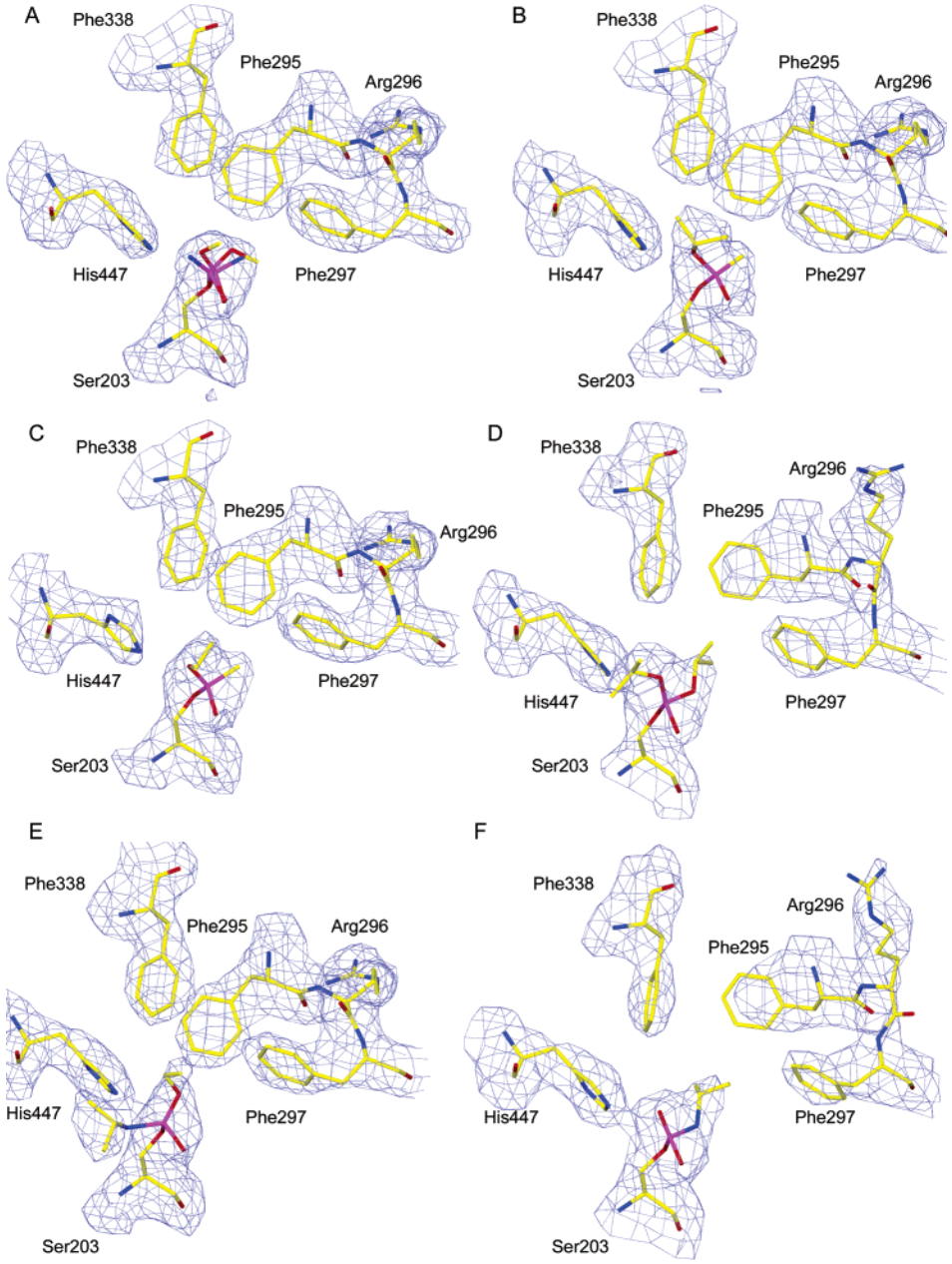

FIGURE 3: Coordination of MeP (A), sarin (B), VX (C), DFP (D), non-aged FeP (E), and aged FeP (F) within the active site of AChE with the $2|F_o| - |F_c|$ electron density map contoured at 1σ (blue). Phosphorus atoms are colored magenta, whereas carbon, nitrogen, and oxygen atoms are colored yellow, blue, and red, respectively.

hole. The tight coordination of the phosphonyl oxygen places one of the phosphonyl substituents in the acyl pocket constituting amino acids Phe295, Phe297, and Phe338, and the remaining substituent directed toward the indole ring of Trp86. In general, the electron density maps of the phosphorus conjugate do not fully resolve the O-alkyl or amide moiety in a $2|F_o| - |F_c|$ contoured at 1σ (Figure 3 and Figure S1 of the Supporting Information), an observation indicative of conformational mobility in this part of the conjugate. Data collection and model refinement statistics are listed in Table 1.

The calculated rmsd values (530 Cα atoms) between the A monomers from the apo structure and the OP-conjugated structures range from 0.18 to 0.45. We observe two different sets of structures: one with low rmsd values (0.18−0.25) and one with slightly larger deviations (rmsd values of 0.41−0.45). The increased rmsd values can be pinpointed to the loop defining the acyl pocket (residues 287−299), which is perturbed in the latter group of structures (mAChE−DFP, mAChE−ADFP, and mAChE−AFeP), as described in the following sections.

Non-Aged Structures of mAChE Inhibited by Methamidophos, Sarin, and VX. The mAChE−MeP, mAChE−sarin, and mAChE−VX crystal structures were determined to a resolution of 2.6, 2.8, and 2.7 Å, respectively (Table 1).

The relatively small substituents of MeP are easily accommodated at the active site of mAChE, and no significant structural distortion of the side chains that define the catalytic site is induced by the conjugate. The small difference in the size of the methoxy and amid substituent in conjunction with the intermediate resolution of the structure causes difficulties in the assignment of the stereochemistry of the conjugate. Moreover, the relative reactivity of the two stereoisomers is not known, and therefore, the

Table 1: Data Collection and Refinement Statistics of Non-Aged Conjugates

	sarin	VX	DFP	MeP	FeP
			Data Collection		
PDB entry	2JGG	2JGH	2JGI	2JGE	2JGF
space group	$P2_12_12_1$	$P2_12_12_1$	$P2_12_12_1$	$P2_12_12_1$	$P2_12_12_1$
unit cell dimensions (Å)	79.33 × 111.68 × 226.59	79.50 × 111.73 × 226.25	78.72 × 109.88 × 226.99	79.66 × 112.33 × 226.52	79.06 × 111.73 × 224.46
resolution range (Å)	19.84−2.80 (2.95−2.80)	19.87−2.70 (2.85−2.70)	29.16−2.90 (3.06−2.90)	19.84−2.60 (2.74−2.60)	19.80−2.50 (2.74−2.50)
total no. of observations	309260 (44230)	414830 (60506)	338193 (49323)	457871 (66601)	513185 (73050)
total no. of unique observations	49785 (7135)	56025 (8088)	45722 (6593)	63268 (9150)	69500 (9962)
completeness	98.9 (98.5)	99.7 (99.7)	99.9 (100.0)	99.8 (100.0)	99.6 (98.8)
multiplicity	6.2 (6.2)	7.4 (7.5)	7.4 (7.5)	7.2 (7.3)	7.4 (7.3)
R_{merge}[a]	0.115 (0.482)	0.104 (0.537)	0.077 (0.384)	0.091 (0.561)	0.078 (0.479)
mean [(I)/sd(I)]	14.9 (4.3)	17.0 (4.3)	21.4 (6.1)	18.6 (4.4)	20.2 (4.6)
			Refinement		
R-factor[b]/R_{free}[c]	18.7/23.7	19.4/24.6	20.2/24.2	19.9/23.3	21.4/25.3
B-factor[d] (Å)	32.9/37.4	39.5/44.0	44.9/50.1	38.9/43.5	40.6/45.1
no. of water molecules	154	157	60	270	175
rmsd from ideal values					
bond lengths (Å)	0.012	0.013	0.010	0.011	0.010
bond angles (deg)	1.441	1.461	1.303	1.368	1.315
Ramachandran plot (%)					
most favored	89.8	88.6	86.7	88.8	89.3
additionally allowed	9.5	10.3	12.7	10.6	10.2
generously allowed	0.7	0.8	0.5	0.5	0.2
disallowed	0	0.2[e]	0.1[e]	0.2[f]	0.2[f]

[a] $R_{merge} = (\sum|I - \langle I\rangle|)/|I|$, where I is the observed intensity and $\langle I\rangle$ is the average intensity obtained after multiple observations of symmetry-related reflections. [b] R-factor $= (\sum||F_o|| - |F_c||)/\sum F_o$, where F_o is the observed and F_c the calculated structure factor. [c] R_{free} uses 2% randomly chosen reflections defined in ref *18*. [d] The B-factor is the mean factor for protein main chain A/B. [e] The residue located in the disallowed regions is Ser203. [f] The residues located in disallowed regions are Ser203, Ser497, and Asp494.

Table 2: Data Collection and Refinement Statistics of Aged Conjugates

	AVX/Asarin	ADFP	AMeP	AFeP
		Data Collection		
PDB entry	2JGL	2JGM	2JGJ	2JGK
space group	$P2_12_12_1$	$P2_12_12_1$	$P2_12_12_1$	$P2_12_12_1$
unit cell dimensions (Å)	79.58 × 111.49 × 227.22	79.71 × 111.26 × 226.99	79.25 × 112.20 × 227.36	79.42 × 111.30 × 227.10
resolution range (Å)	28.77−2.60 (2.74−2.60)	29.89−2.90 (3.06−2.90)	29.70−2.50 (2.64−2.50)	20.00−2.900 (3.06−2.90)
total no. of observations	414219 (60430)	337190 (49107)	520508 (75616)	330854 (48261)
total no. of unique observations	64074 (9128)	45500 (6548)	69923 (10058)	45507 (6575)
completeness	99.9 (100.0)	99.9 (100.0)	99.5 (99.3)	99.7 (100.0)
multiplicity	6.6 (6.6)	7.4 (7.5)	7.4 (7.5)	7.3 (7.3)
R_{merge}[a]	0.080 (0.431)	0.086 (0.374)	0.057 (0.372)	0.084 (0.391)
mean [(I)/sd(I)]	18.9 (5.1)	19.8 (5.6)	23.9 (6.4)	19.3 (5.7)
		Refinement		
R-factor[b]/R_{free}[c]	19.9/24.0	19.8/24.2	21.4/24.4	20.4/25.3
B-factor[d] (Å)	38.1/43.3	45.2/49.2	43.7/48.9	51.8/56.4
no. of water molecules	306	92	177	63
rmsd from ideal values				
bond lengths (Å)	0.012	0.011	0.011	0.010
bond angles (deg)	1.347	1.381	1.305	1.327
Ramachandran plot (%)				
most favored	89.2	86.9	89.6	86.8
additionally allowed	10.1	12.9	10.0	12.8
generously allowed	0.5	0.0	0.2	0.2
disallowed	0.2[e]	0.2[e]	0.2[e]	0.2[e]

[a] $R_{merge} = (\sum|I - \langle I\rangle|)/\sum I$, where I is the observed intensity and $\langle I\rangle$ is the average intensity obtained after multiple observations of symmetry-related reflections. [b] R-factor $= (\sum||F_o| - |F_c||)/\sum F_o$, where F_o is the observed and F_c the calculated structure factor. [c] R_{free} uses 2% randomly chosen reflections defined in ref *18*. [d] The B-factor is the mean factor for protein main chain A/B. [e] The residue located in the disallowed regions is Ser203.

final model comprises both species, each with the occupancy set to 0.5 (Figure 4A,B). Consequently, the P[R] stereoisomer of the enantiomeric pair of MeP is coordinated with the amid moiety in the acyl pocket of Phe295, Phe297, and Phe338 and the methoxy group directed toward the indole ring of Trp86 (Figure 4A), whereas the P[S] stereoisomer has the opposite coordination (Figure 4B). In both cases, phosphonyl O1 is coordinated with hydrogen bonds to Gly121 (3.1 and 3.0 Å), Gly122 (2.7 and 2.8 Å), and Ala204 (2.9 and 2.8 Å).

In contrast to MeP, we were able to assign the stereochemistry of the sarin conjugate to P[S] on the basis of the features of the electron density map. The phosphonyl oxygen of sarin is coordinated within hydrogen bonding distance of

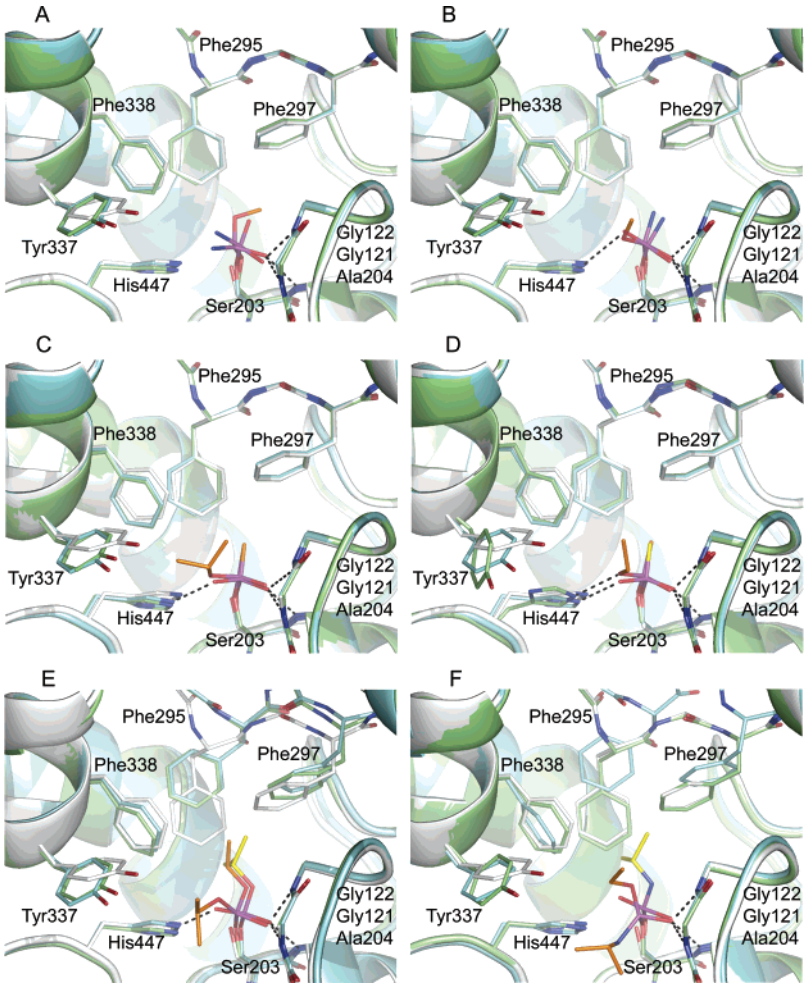

FIGURE 4: Structural alignment of the apo form of mAChE (gray) and the non-aged (lime) and aged (cyan) conjugates of MeP (A and B), sarin (C), VX (D), DFP (E), and FeP (F). The non-aged OP is colored orange and the aged OP yellow, whereas the phosphorus, nitrogen, and oxygen atoms are colored magenta, blue, and red, respectively.

the main chain nitrogen of Gly121 (2.7 Å), Gly122 (2.5 Å), and Ala204 (3.2 Å) (Figure 4C). The methyl group is accommodated in the acyl pocket of Phe295, Phe297, and Phe338, whereas the isopropoxy group is directed toward the indole ring of Trp86. In this position, the oxygen of the isopropoxy moiety disrupts the catalytic triad by forming a 3.2 Å hydrogen bond to the imidazole ring of His447 and a 3.3 Å hydrogen bond to a water molecule (Wat79). This water molecule is conserved in the noninhibited form of mAChE (*1*). No significant structural changes of residues lining the catalytic site are observed in the mAChE−sarin structure.

The conjugate of VX (stereoisomer P[R]) is coordinated in a fashion similar to that of mAChE−sarin, with O1 forming hydrogen bonds to the oxyanion hole of Gly121 (2.8 Å), Gly122 (2.7 Å), and Ala204 (2.9 Å), the methyl group accommodated in the acyl pocket, and the ethoxy group facing Trp86 (Figure 4D). O2 of the ethoxy group forms a 2.8 Å hydrogen bond to the imidazole ring of His447, an interaction facilitated by a limited structural change that involves a 180° rotation of the imidazole ring of His447 and an 85° rotation around the χ_1 axis in a protein structure that is otherwise conserved. The structural distortion of His447 disrupts the hydrogen bonding network of the catalytic triad.

Non-Aged Structures of mAChE Inhibited by Fenamiphos and DFP. The crystal structures described in this section, non-aged conjugates of fenamiphos (mAChE−FeP) and DFP (mAChE−DFP), were determined to a resolution of 2.5 and 2.9 Å, respectively (Table 1). The main chain Cα trace of the mAChE−FeP conjugate is similar to the apo structure (rmsd of 0.25 Å) with a well-defined density of all residues in the active site gorge and catalytic site. Phosphonyl O1 forms hydrogen bonds to main chain nitrogens in the oxyanion hole as in previously described structures, whereas Nϵ2 of His447 does not interact directly with the OP conjugates, leaving the hydrogen bonding network of the catalytic triad intact (Figure 3E). The large amid moiety of FeP is positioned in the vicinity of Trp86, whereas the ethoxy group is occupying a pocket between Tyr124 and Phe338, indicative of a P[S] stereochemistry. Both substituents of the FeP molecule are identifiable in the electron density at a contour level of 1σ (Figure 3E).

In contrast to the previously described asymmetrical conjugates, DFP contains two isopropoxy groups, which are positioned in the acyl pocket and in the choline-binding site, respectively. The tracing of the acyl pocket loop (residues 286−299) is distorted compared to the apo structure with a movement of up to 5.5 Å for the main chain (Pro290 Cα) (Figure 4E). The acyl pocket residues Phe295 and Phe297 move to accommodate the relatively large isopropoxy group. For Phe295, we observe both a retraction and a rotation of the side chain with a movement of up to 4.1 Å for the Cϵ1

atom compared to apo (Cα is moved 2.1 Å) (Figure 3D). Phe297 also experiences a distortion, but to a lesser extent than Phe295 (up to 1 Å for the side chain) (Figure 4E). Arg296 rotates to a position close to the one previously described for the TcAChE−DFP conjugate, i.e., placed between Trp286 and Glu292 in the acyl pocket loop (*23*). Phosphonyl O1 is hydrogen bonded to the main chain nitrogen of Gly121 (2.7 Å), Gly122 (2.5 Å), and Ala204 (2.9 Å).

Aged Structures of mAChE Inhibited by Methamidophos, Sarin, and VX. During aging, elimination of the leaving group reduces the size and subsequently the steric impact of the conjugates. Therefore, in the case of VX, sarin, and methamidophos, the catalytic site is undistorted with an apo conformation of all active site residues. From our crystallographic studies, elimination of the methoxy moiety of MeP seems feasible (Figure 3A) and was assumed during the refinement of the final model. However, at the current resolution (2.5 Å), we cannot unambiguously assign the aging product, and its absolute identity must be verified using other methods. The small difference in the shape between the amid moiety and the two phosphonyl oxygens results in difficulties in identifying the absolute coordination of the amid moiety, and therefore, both possible enantiomers were refined. In mAChE−AMeP, O1 of the OP conjugate interacts via hydrogen bonds with the oxyanion hole with distances similar to those for the previously described structures. O2 from mAChE−AMeP is weakly hydrogen bonded to His447 (distance of 3.3 Å), whereas the amid moiety is accommodated in the acyl pocket of Phe295 and Phe297. The alternative coordination with the amid moiety directed toward His447 results in a distance of 3.5 Å between the nitrogen atoms. With this coordination, O2 is directed toward the acyl pocket.

During aging, elimination of the isopropoxy group of sarin and the ethoxy group of VX leads to identical anionic end products that will be described as mAChE−AVX/Asarin (*12*). The methyl moiety of AVX/Asarin is directed toward the acyl pocket with stabilizing hydrophobic interactions. The distance between C1 in the mAChE−AVX/Asarin conjugate and Cζ of Phe297 is 3.4 Å and Cε1 of Phe295 is 3.7 Å. O2 in the mAChE−AVX/Asarin conjugate structure forms a 3.0 Å hydrogen bond to Nε2 of His447, which results in a disruption of the catalytic triad and a stabilization of the anionic aged conjugate.

Aged Structures of mAChE Inhibited by DFP and Fenamiphos. The crystal structures of mAChE−ADFP and mAChE−AFeP were both determined to a resolution of 2.9 Å (Table 1). In ADFP, one of the isopropoxy groups has been eliminated and the remaining group was accommodated in the acyl pocket. The mAChE−ADFP structure exhibits a main chain conformation that is similar to the mAChE−DFP structure with the loop containing Phe295 and Phe297 retracted to accommodate the large isopropoxy moiety (Figure 4E). The side chain of Phe295 is distorted up to 4.1 Å (Cε1 atom) with a Cα movement of 1.9 Å compared to the apo form (Figure 4F). Also, Phe297 in mAChE−ADFP has rotated 45° and has moved 2.1 Å compared to that in the apo structure. Close interactions between the isopropoxy moiety and the acyl pocket result in energetically unfavorable contacts. The steric constraints in this region of the protein result in a noncompletely resolved electron density for parts of the Phe295 side chain and the isopropoxy group of ADFP (Figure S1 of the Supporting Information). The electron density map of the phosphorus conjugate shows that phosphonyl O2 is directed toward the indole ring of Trp86, forming a 2.8 Å hydrogen bond to His447. Interestingly, the acyl pocket loop of the B monomer shows a more extended distortion than the corresponding region of the A monomer, with movements of Phe295 up to 4.3 Å (Cε1 atom) and a Cα distortions of 3.0 Å (numbers are in comparison with the apo structure). Otherwise, the structures are similar between the two monomers in the asymmetric unit, and the conjugates are also positioned similarly.

In the non-aged structure of mAChE inhibited by fenamiphos described above, the ethoxy moiety of the phosphorus conjugate is accommodated between Tyr124 and Phe338 and no significant structural distortion of the protein main chain is observed. In the corresponding aged conjugate, a clearly defined rearrangement of the acyl pocket loop has occurred so that it is found in a position similar to that described for the mAChE−DFP and mAChE−ADFP complexes (compare panels D and F of Figure 3 and panels E and F of Figure 4). The movements of Phe295 (up to 4.4 Å for the side chain) and Phe297 (a rotation and a side chain movement of up to 2.3 Å) are comparable to the distortions of the DFP complexes (Figure 3D,F). The phosphorus substituents of the aged FeP conjugate are not fully resolved in the electron density map, and the interpretation is further complicated by the absence of mass spectrometric data of the aging product identity. Several attempts to improve the resolution were unsuccessful. This may be due to the energetically unfavorable conformation of the acyl loop. To identify the aging product, we have refined and evaluated both possible aging products. Our conclusion from these studies is that aging occurs via elimination of the ethoxy group. The conclusion is based on the following observations and arguments. (1) The structural change in the acyl loop region of mAChE−AFeP is very similar to the distortions of the corresponding region in mAChE−DFP and mAChE−ADFP, suggesting an acyl pocket substituent similar in size (Figure S1 of the Supporting Information). (2) The isopropoxy substituent of DFP and the isopropyl amino moiety of FeP are similar in size, whereas the ethoxy group of non-aged FeP is smaller. (3) The electron density map of the acyl pocket substituents of DFP and aged FeP is similar in dimensions, indicating a similar size of the substituents. The phosphorus conjugate is further coordinated by a 3.1 Å hydrogen bond between Nε2 of His447 and N1 of FeP and by hydrogen bonds between the phosphonyl oxygen and the oxyanion hole of Gly121, Gly122, and Ala204.

B-Factor Comparison. The structures of the mAChE−DFP, mAChE−ADFP, and mAChE−AFeP conjugates have an obvious peak in the *B*-factor plot (70−92 Å^2) for the acyl pocket loop (residues 290−297) (Figure 5). This peak is not observed in protein structures with the apo conformation, where the *B*-factors are significantly lower (40−60 Å^2). The increased temperature factors are indicative of the large distortion and conformational flexibility of this loop. To confirm the structural change in the acyl loop region, we executed a refinement using the apo conformation of residues 290−297, leading to an incompletely resolved electron density and very high *B*-factor values (data not shown). Thus, the acyl loop conformations described in the structures of

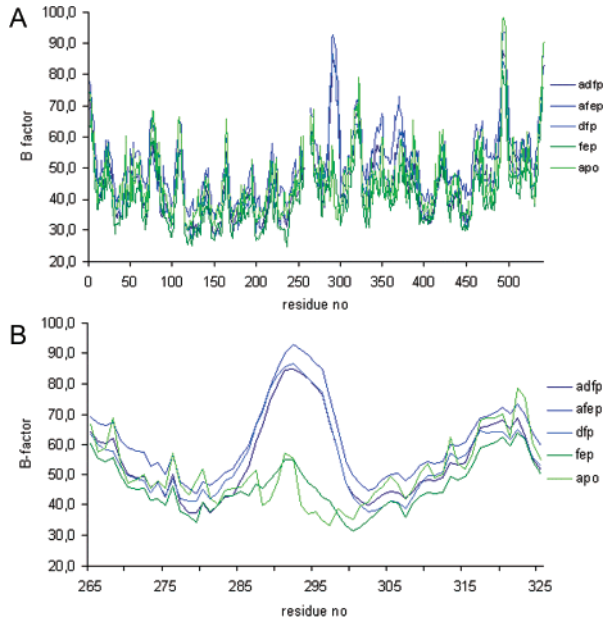

FIGURE 5: Comparison of the *B*-factors throughout the entire protein (A), clearly showing an increase in the acyl loop region (B, residues 287−299) of mAChE−DFP, mAChE−ADFP, and mAChE−AFeP.

mAChE−DFP, mAChE−ADFP, and mAChE−AFeP are clearly defined by both the electron density map and the increased *B*-factor values.

DISCUSSION

In this study, we have determined the crystal structures of mAChE in complex with the non-aged and aged conjugates of methamidophos, VX, sarin, DFP, and fenamiphos (Figure 1B). With respect to induced structural changes of AChE, the OP compounds described in this study are divided into four different categories. (1) Conjugates of MeP and sarin maintain an apo conformation of the catalytic site region in both the non-aged and aged structures (Figure 4A−C). (2) Conjugates of VX display a structural distortion in the non-aged form, whereas the aged structure is very similar to the apo conformation (Figure 4D). (3) Conjugates of FeP demonstrate an apo conformation in the non-aged form and a distorted conformation of the aged conjugate (Figure 4F). (4) Conjugates of DFP show a structural distortion in both the non-aged and aged structures (Figure 4E). A previously described X-ray structure of mAChE inhibited by tabun, an OP compound structurally related to MeP and FeP (Figure 1B), belongs to the second category of conjugates (i.e., structural change only in the non-aged form) (*13*). These conjugates represent different rates of aging and also different degrees of resistance toward oxime-mediated reactivation (*2*). For instance, in hAChE, DFP and sarin have a short aging half-time $t_{1/2}$ (ca. 3 h), MeP, tabun, and VX have intermediate aging half-times of ca. 10, 19, and 37 h, respectively, and FeP has a relatively long aging half-time of 130 h (*2*). Considering the resistance of conjugates toward reactivation, tabun, FeP, and DFP are very difficult to reactivate compared to MeP, which is easy to reactivate with most oximes, and to VX and sarin, which form an intermediate group which can be effectively reactivated by some but not all oximes (*2*). The differences in the rate of aging and resistance toward reactivation depend on both electronic and structural properties of the phosphorus conjugate as well as the structural and electronic framework that accommodates the conjugate and the reactivator. A main feature of OP conjugates is the three hydrogen bonds between the phosphonyl oxygen and the oxyanion hole that restrain the conjugates within the catalytic site. This leads to stereochemical preferences in inhibition and reactivation reactions as shown for metylphosphonates (*6*, *8*, *24*, *25*). The strong interactions between the phosphonyl oxygen and the oxyanion hole prevent compensatory movements of the phosphorus conjugate during reactions, suggesting that large substituents may be accommodated only within the acyl pocket if the acyl loop region undergoes a structural change.

Aging kinetics of OP conjugates bound to the human protein presented by Worek and co-workers (*2*) in combination with the presented crystal structures of the murine enzyme provide a foundation for a mechanistic discussion of reactions at the phosphorus atom. Two different mechanisms of aging have been suggested, namely, nucleophilic attack on the phosphorus atom and elimination via the formation of a carbocation intermediate. Reaction at a phosphorus atom is favored when an attacking nucleophile and a leaving group occupy the apical and proximal positions of a trigonal bipyramidal transition state (for a review, see ref *26*) (Figure S2 of the Supporting Information). The nucleophile and the leaving group do not have to be in these positions at the moment of the attack since a pseudorotation may position the phosphorus substituents in a favorable trigonal bipyramid. The end product of the nucleophilic attack has also undergone an inversion of phosphorus substituents.

Aging of soman proceeds via the alternative mechanism, which involves the formation of a carbocation, a reaction stabilized by the indole ring of Trp86 (*27*−*29*). This results in very rapid aging ($t_{1/2} \sim 0.1$ h) that does not involve any reaction at the phosphorus atom. Compared to the large pinacolyl moiety of soman [$(CH_3)_3CCH(CH_3)OP(O)(CH_3)F$], the OP compounds in this study have smaller substituents that are positioned farther from Trp86 (the closest atom is ∼4.4 Å from the indole ring of Trp86 to the C2 atom of FeP). It seems therefore unlikely that Trp86 can stabilize the formation of a carbocation in the case of MeP, sarin, VX, and DFP. Moreover, the formation of unbranched carbocations is energetically unfavorable. Our structural analysis of the aging reaction of FeP suggests a reorganization of the phosphorus substituents, which is most consistent with the nucleophilic attack mechanism. Aging of the FeP conjugate induces a drastic retraction of the acyl pocket loop of AChE, enforced by the positioning of a relatively large phosphorus substituent into the acyl pocket (Figure 4F). The structural analysis of mAChE−AFeP suggests that the large substituent corresponds to the isopropylamino group. The structural change results in significantly elevated temperature factors in the acyl pocket loop region (Figure 5). The pseudorotation or inversion of the isopropylamino moiety of the FeP conjugate is sterically hindered by restraints of the apo conformation acyl loop of the non-aged conjugate, which may explain why FeP undergoes the aging reaction at a slow rate. Thus, steric constraints of the acyl pocket are likely to affect the rate of aging but may not alone distinguish between the two aging mechanisms. The structural data of mAChE−FeP and mAChE−AFeP provide the foundation for our hypothesis; the acyl loop region precludes the

formation, pseudorotation, or inversion of the trigonal bipyramidal transition state during the FeP aging reaction.

In an aged complex of DFP and TcAChE, a large structural change in the acyl pocket loop was observed (*23*). The conformation of the acyl pocket loop in TcAChE−ADFP is similar to the conformation in our structure of mAChE−ADFP. In the murine enzyme, we observe structural changes in the acyl pocket loop in both the non-aged and aged complexes of DFP. Assuming that DFPs age by a mechanism similar to that of FeP, the aging reaction can proceed without any further structural changes in the acyl loop, and consequently, DFPs have a relatively fast aging reaction ($t_{1/2} \sim 3$ h). By comparing the inhibition rate constant of OP compounds with fluoride as a leaving group and with different phosphorus substituents, Worek and co-workers found that butylsarin, cyclosarin, sarin, and soman have inhibition rate constants 200−4000 times higher than that of DFP in hAChE (*2*). The lower inhibition rate constant of DFP may be due to the distortion of the acyl pocket that is necessary to accommodate the isopropoxy group of DFP. The aging reactions of sarin, DFP, and VX proceed through elimination of an isopropoxy (sarin and DFP) or ethoxy group (VX), and no structural rearrangement of the remaining groups is observed. Still, this does not exclude the nucleophilic attack mechanism since a pseudorotation of the equatorial ligands of the trigonal bipyramidal intermediate may be possible.

At this resolution, we cannot unambiguously assign which group of MeP that is eliminated upon aging, whereas structural data indicate that the ethoxy group is eliminated in the FeP conjugate (Figures 1 and 4F). In this respect, it is intriguing that tabun, which is analogous to MeP and FeP in that it also has a P−N bond, has been shown to age through elimination of the dimethylamine moiety (*30*, *31*). Apparently, not only the nature of the phosphorus substituents but also other steric, chemical, and electrostatic factors of the protein influence the aging pathway and the transition from the P−N bond scission in tabun to the P−O bond scission in FeP.

Analogous to the aging reaction of FeP, the oxime-mediated reactivation reaction proceeds via the trigonal bipyramidal intermediate, suggesting that similar sterical constraints apply in both the aging and the reactivation reactions. Kinetic and structural analyses of oxime-based reactivators suggest that the attack occurs from the choline-binding site or the acyl pocket (*14*, *32*, *33*). In the case of DFP and FeP, which are both very difficult to reactivate (*2*), there is a large isopropoxy group and a similarly large isopropylamino group (Figures 1B, 2, and 4E,F), respectively, accommodated in the choline-binding site, implicating that steric exclusion may avert the reactivation reaction. However, this theory is challenged by sarin that also has an isopropoxy group in the choline-binding site but still can be reactivated by some oximes (*2*). The most obvious difference in the size of the substituents between conjugates of DFP and sarin is that sarin (phosphonate) is coordinated with a methyl group in the acyl pocket whereas DFP (phosphate) has a larger isopropoxy group in the corresponding position (Figure 1B). Soman-inhibited AChE can also be reactivated with HI-6 even though one of the substituents is significantly larger than the isopropoxy groups of sarin and DFP (*34*). It has been shown for a series of mAChE−OP conjugates with an increasing number of carbons and/or branching in one of the substituents (where the other substituent was methyl) that going from an ethoxy group to an isopropoxy group and further to a pinacolyl group only slightly reduced the reactivation rate constant for HI-6-mediated reactivation (*33*). If, on the other hand, the second substituent was changed from a methyl group to an ethoxy group, the ability to reactivate was reduced by 22%. The kinetic and structural data described above suggest that two large substituents on the phosphorus atom induce tight steric constraints in the acyl pocket, thereby precluding formation, pseudorotation, or inversion of the trigonal bipyramidal transition state. Ultimately, this prevents a favorable positioning of the proximal, apical, and equatorial ligands.

The crystal structures of the reactivators Obidoxime and Ortho-7 in complex with nonphosphorylated AChE have been determined, and the attacking oximates were positioned between the choline-binding site (residue Tyr337) and the acyl pocket (residue Phe338) (*14*). When modeling these oximes into our crystal structures, we found steric clashes with FeP and DFP, but not with MeP (data not shown), indicating a reduced affinity for an inhibited enzyme with a large phosphorus substituent in this position. Another mechanism contributing to the resistance toward reactivation was suggested by the crystal structure of non-aged mAChE−tabun, where a structural change placed the side chain of Phe338 into the active site gorge, thereby reducing the accessibility of reactivators (*13*). Since tabun is quite similar to both DFP and FeP with two relatively large phosphorus substituents, it seems likely that both steric hindrance by Phe338 and steric constraint by the acyl loop limit the reactivation. To conclude, there seems to be at least two independent steric mechanisms for resistance toward reactivation by medical antidotes: one in which two large substituents prevent the formation or pseudorotation of the trigonal bipyramid and a second mechanism in which structural changes in the active site gorge limit the accessibility of reactivators (*13*).

Intriguingly, we observe a movement of the imidazole ring of His447 in the non-aged conjugate of mAChE−VX. The side chain rotates 180° around the χ_2 axis and moves toward Tyr337, thereby disrupting the hydrogen bonding network of the catalytic triad. Various kinetic constants have been shown to exhibit a pronounced species dependency (*9*, *10*); however, a similar movement of His447 has previously been observed in the non-aged VX conjugate determined in complex with TcAChE (*12*). We observe a small structural difference between TcAChE−VX and mAChE−VX; namely, in the mouse enzyme, a hydrogen bond between His447 and the OP conjugate is present. The mobility of the imidazole ring in histidine residues during serine protease activity has previously been discussed (*12*, *35*, *36*), which may indicate that the histidine has been trapped in an alternative conformation in mAChE−VX, which is reversed upon aging (mAChE−AVX/Asarin and TcAChE−AVX) (*12*).

A group of organophosphorus conjugates are known to undergo spontaneous reactivation via a mechanism that most likely resembles the deacylation step of the normal catalytic reaction. During spontaneous reactivation, Nϵ2 of His447 has been suggested to act as a general base and polarize an attacking water molecule (*12*, *23*). The rate of spontaneous reactivation is in general low except for one of the

compounds of this study, MeP, with a rate of ~3 h in hAChE (*2*). It has been suggested that steric exclusion of the attacking water molecule prevents efficient spontaneous reactivation (*37*). This hypothesis is consistent with our data for mAChE−MeP that show that the small phosphorus substituents do not significantly exclude attacking water molecules. Moreover, the small substituents of MeP can easily form the required trigonal bipyramidal intermediate without experiencing any steric restriction from the acyl loop. Analogous to MeP, the conjugated VX has relatively small phosphorus substituents (Figure 1) and, accordingly, a noticeable spontaneous reactivation ($t_{1/2} \sim 33$ h) (*2*). It has been suggested that a hydrogen bond between the imidazole ring of His447 and the OP conjugate prevents Nϵ2 of His447 from acting like a catalytic base (*38*). In mAChE−MeP, His447 is found in a conformation that is unfavorable for a hydrogen bond to the MeP conjugate, whereas the structures of mAChE−sarin, mAChE−VX, and mAChE−DFP clearly reveal the presence of an immobilized His447. In conjugates of VX, is seems likely that this hydrogen bond reduces the rate of spontaneous reactivation. Interestingly, the crystal structure of mAChE−FeP shows no hydrogen bond between His447 and the OP conjugate. However, in this case, we suggest that the tight steric constraints of the acyl loop prevent formation of trigonal bipyramidal intermediates, thereby averting the spontaneous reactivation.

To summarize, the most important finding of this study is the structural support to an aging mechanism that proceeds through a nucleophilic attack on the phosphorus atom and the formation of a pentacoordinated, trigonal bipyramidal intermediate. On the basis of this observation, we suggest that the acyl pocket loop modulates the rate of aging by preventing either the formation, pseudorotation, or the inversion of the phosphorus intermediate. Analogous to the aging reaction, both oxime-mediated and spontaneous reactivations require the formation of a trigonal bipyramidal intermediate, suggesting a similar role for the acyl loop region during these reactions.

ACKNOWLEDGMENT

We thank Dr. Yngve Cerenius for the assistance at beamline I711 at the MAX lab synchrotron. We are also grateful for the valuable feedback by our reviewers.

SUPPORTING INFORMATION AVAILABLE

Electron density map of mAChE−AMeP (A), mAChE−AVX/sarin (B), and mAChE−ADFP (C) (Figure S1) and a model of a tetracoordinated phosphorus (A) and a hypothetical pentacoordinated trigonal bipyramidal intermediate (B) (Figure S2). This material is available free of charge via the Internet at http://pubs.acs.org.

REFERENCES

1. Bourne, Y., Taylor, P., Radic, Z., and Marchot, P. (2003) Structural insights into ligand interactions at the acetylcholinesterase peripheral anionic site, *EMBO J. 22*, 1−12.
2. Worek, F., Thiermann, H., Szinicz, L., and Eyer, P. (2004) Kinetic analysis of interactions between human acetylcholinesterase, structurally different organophosphorus compounds and oximes, *Biochem. Pharmacol. 68*, 2237−2248.
3. Hosea, N. A., Radic, Z., Tsigelny, I., Berman, H. A., Quinn, D. M., and Taylor, P. (1996) Aspartate 74 as a primary determinant in acetylcholinesterase governing specificity to cationic organophosphonates, *Biochemistry 35*, 10995−11004.
4. Taylor, P., Hosea, N. A., Tsigelny, I., Radic, Z., and Berman, H. A. (1997) Determining ligand orientation and transphosphonylation mechanisms on acetylcholinesterase by Rp, Sp enantiomer selectivity and site-specific mutagenesis, *Enantiomer 2*, 249−260.
5. Taylor, P., Wong, L., Radic, Z., Tsigelny, I., Bruggemann, R., Hosea, N. A., and Berman, H. A. (1999) Analysis of cholinesterase inactivation and reactivation by systematic structural modification and enantiomeric selectivity, *Chem.-Biol. Interact. 119*−*120*, 3−15.
6. Kovarik, Z., Radic, Z., Berman, H. A., Simeon-Rudolf, V., Reiner, E., and Taylor, P. (2003) Acetylcholinesterase active centre and gorge conformations analysed by combinatorial mutations and enantiomeric phosphonates, *Biochem. J. 373*, 33−40.
7. Kovarik, Z., Radic, Z., Berman, H. A., Simeon-Rudolf, V., Reiner, E., and Taylor, P. (2004) Mutant cholinesterases possessing enhanced capacity for reactivation of their phosphonylated conjugates, *Biochemistry 43*, 3222−3229.
8. Ordentlich, A., Barak, D., Sod-Moriah, G., Kaplan, D., Mizrahi, D., Segall, Y., Kronman, C., Karton, Y., Lazar, A., Marcus, D., Velan, B., and Shafferman, A. (2004) Stereoselectivity toward VX is determined by interactions with residues of the acyl pocket as well as of the peripheral anionic site of AChE, *Biochemistry 43*, 11255−11265.
9. Talbot, B. G., Anderson, D. R., Harris, L. W., Yarbrough, L. W., and Lennox, W. J. (1988) A comparison of in vivo and in vitro rates of aging of soman-inhibited erythrocyte acetylcholinesterase in different animal species, *Drug Chem. Toxicol. 11*, 289−305.
10. Worek, F., Reiter, G., Eyer, P., and Szinicz, L. (2002) Reactivation kinetics of acetylcholinesterase from different species inhibited by highly toxic organophosphates, *Arch. Toxicol. 76*, 523−529.
11. Sussman, J. L., Harel, M., Frolow, F., Oefner, C., Goldman, A., Toker, L., and Silman, I. (1991) Atomic structure of acetylcholinesterase from *Torpedo californica*: A prototypic acetylcholine-binding protein, *Science 253*, 872−879.
12. Millard, C. B., Koellner, G., Ordentlich, A., Shafferman, A., Silman, I., and Sussman, J. L. (1999) Reaction Products of Acetylcholinesterase and VX Reveal a Mobile Histidine in the Catalytic Triad, *J. Am. Chem. Soc. 121*, 9883−9884.
13. Ekström, F., Akfur, C., Tunemalm, A.-K., and Lundberg, S. (2006) Structural changes of phenylalanine 338 and histidine 447 revealed by the crystal structures of tabun-inhibited murine acetylcholinesterase, *Biochemistry 45*, 74−81.
14. Ekström, F., Pang, Y. P., Boman, M., Artursson, E., and Börjegren, S. (2006) Crystal structures of acetylcholinesterase in complex with HI-6, Ortho-7 and obidoxime: Structural basis for differences in the ability to reactivate tabun conjugates, *Biochem. Pharmacol. 72*, 597−607.
15. Kabsch, W. (1993) Automatic processing of rotation diffraction data from crystals of initially unknown symmetry and cell constants, *J. Appl. Crystallogr. 26*, 795−800.
16. Kabsch, W. (1988) Evaluation of single-crystal X-ray diffraction data from a position-sensitive detector, *J. Appl. Crystallogr. 21*, 916−924.
17. Murshudov, G. N., Vagin, A. A., and Dodson, E. J. (1997) Refinement of Macromolecular Structures by the Maximum-Likelihood Method, *Acta Crystallogr. D53*, 240−255.
18. Brunger, A. T. (1992) Free *R* value: A novel statistical quantity for assessing the accuracy of crystal structures, *Nature 355*, 472−474.
19. Jones, T. A., Zou, J. Y., Cowan, S. W., and Kjeldgaard, M. (1991) Improved methods for building protein models in electron density maps and the location of errors in these models, *Acta Crystallogr. A47* (Part 2), 110−119.
20. Laskowski, R. A., MacArthur, M. W., Moss, D. S., and Thornton, J. M. (1993) PROCHECK: A program to check the stereochemical quality of protein structures, *J. Appl. Crystallogr. 26*, 283−291.
21. Vriend, G. (1990) WHAT IF: A molecular modelling and drug design program, *J. Mol. Graphics Modell. 8*, 52−56.
22. Harris, M., and Jones, T. A. (2001) Molray: A web interface between O and the POV-Ray ray tracer, *Acta Crystallogr. D57*, 1201−1203.
23. Millard, C. B., Kryger, G., Ordentlich, A., Greenblatt, H. M., Harel, M., Raves, M. L., Segall, Y., Barak, D., Shafferman, A., Silman, I., and Sussman, J. L. (1999) Crystal structures of aged phosphonylated acetylcholinesterase: Nerve agent reaction products at the atomic level, *Biochemistry 38*, 7032−7039.

24. Ordentlich, A., Barak, D., Kronman, C., Benschop, H. P., De Jong, L. P., Ariel, N., Barak, R., Segall, Y., Velan, B., and Shafferman, A. (1999) Exploring the active center of human acetylcholinesterase with stereomers of an organophosphorus inhibitor with two chiral centers, *Biochemistry 38*, 3055−3066.
25. Wong, L., Radic, Z., Bruggemann, R. J., Hosea, N., Berman, H. A., and Taylor, P. (2000) Mechanism of oxime reactivation of acetylcholinesterase analyzed by chirality and mutagenesis, *Biochemistry 39*, 5750−5757.
26. Hall, C. R., and Inch, T. D. (1980) Phosphorus stereochemistry: Mechanistic implications of the observed stereochemistry of bond forming and breaking process at phosphorus in some 5- and 6-membered cyclic phosphorus esters, *Tetrahedron 36*, 2059−2095.
27. Shafferman, A., Ordentlich, A., Barak, D., Stein, D., Ariel, N., and Velan, B. (1996) Aging of phosphylated human acetylcholinesterase: Catalytic processes mediated by aromatic and polar residues of the active centre, *Biochem. J. 318* (Part 3), 833−840.
28. Barak, D., Ordentlich, A., Segall, Y., Velan, B., Benschop, H. P., De Jong, L. P., and Shafferman, A. (1997) Carbocation-Mediated Processes in Biocatalysts. Contribution of Aromatic Moieties, *J. Am. Chem. Soc. 119*, 3157−3158.
29. Viragh, C., Kovach, I. M., and Pannell, L. (1999) Small molecular products of dealkylation in soman-inhibited electric eel acetylcholinesterase, *Biochemistry 38*, 9557−9561.
30. Barak, D., Ordentlich, A., Kaplan, D., Barak, R., Mizrahi, D., Kronman, C., Segall, Y., Velan, B., and Shafferman, A. (2000) Evidence for P−N bond scission in phosphoroamidate nerve agent adducts of human acetylcholinesterase, *Biochemistry 39*, 1156−1161.
31. Elhanany, E., Ordentlich, A., Dgany, O., Kaplan, D., Segall, Y., Barak, R., Velan, B., and Shafferman, A. (2001) Resolving pathways of interaction of covalent inhibitors with the active site of acetylcholinesterases: MALDI-TOF/MS analysis of various nerve agent phosphyl adducts, *Chem. Res. Toxicol. 14*, 912−918.
32. Ashani, Y., Radic, Z., Tsigelny, I., Vellom, D. C., Pickering, N. A., Quinn, D. M., Doctor, B. P., and Taylor, P. (1995) Amino acid residues controlling reactivation of organophosphonyl conjugates of acetylcholinesterase by mono- and bisquaternary oximes, *J. Biol. Chem. 270*, 6370−6380.
33. Luo, C., Leader, H., Radic, Z., Maxwell, D. M., Taylor, P., Doctor, B. P., and Saxena, A. (2003) Two possible orientations of the HI-6 molecule in the reactivation of organophosphate-inhibited acetylcholinesterase, *Biochem. Pharmacol. 66*, 387−392.
34. Puu, G., Artursson, E., and Bucht, G. (1986) Reactivation of nerve agent inhibited human acetylcholinesterases by HI-6 and obidoxime, *Biochem. Pharmacol. 35*, 1505−1510.
35. Bachovchin, W. W. (1986) ^{15}N NMR spectroscopy of hydrogen-bonding interactions in the active site of serine proteases: Evidence for a moving histidine mechanism, *Biochemistry 25*, 7751−7759.
36. Bone, R., Sampson, N. S., Bartlett, P. A., and Agard, D. A. (1991) Crystal structures of α-lytic protease complexes with irreversibly bound phosphonate esters, *Biochemistry 30*, 2263−2272.
37. Steitz, T. A., Henderson, R., and Blow, D. M. (1969) Structure of crystalline α-chymotrypsin. 3. Crystallographic studies of substrates and inhibitors bound to the active site of α-chymotrypsin, *J. Mol. Biol. 46*, 337−348.
38. Kovach, I. M. (1988) Structure and dynamics of serine hydrolase-organophosphate adducts, *J. Enzyme Inhib. 2*, 199−208.

BI0621361